Materials Research Letters

ISSN: 2166-3831 (Online) Journal homepage: www.tandfonline.com/journals/tmrl20

# Stabilization of metal(II)oxides on the nanoscale

Boyi Qu, Cecile S. Bonifacio, Hasti Majidi & Klaus van Benthem

**To cite this article:** Boyi Qu, Cecile S. Bonifacio, Hasti Majidi & Klaus van Benthem (2020) Stabilization of metal(II)oxides on the nanoscale, Materials Research Letters, 8:1, 41-47, DOI: 10.1080/21663831.2019.1684395

**To link to this article:** https://doi.org/10.1080/21663831.2019.1684395

© 2019 The Author(s). Published by Informa UK Limited, trading as Taylor & Francis Group

View supplementary material

Published online: 07 Nov 2019.

Submit your article to this journal

Article views: 1590

View related articles

View Crossmark data

Citing articles: 3 View citing articles

Full Terms & Conditions of access and use can be found at
https://www.tandfonline.com/action/journalInformation?journalCode=tmrl20

MATER. RES. LETT.
2020, VOL. 8, NO. 1, 41–47
https://doi.org/10.1080/21663831.2019.1684395

MATERIALS RESEARCH LETTERS
Taylor & Francis
Taylor & Francis Group

ORIGINAL REPORT

OPEN ACCESS
Check for updates

# Stabilization of metal(II)oxides on the nanoscale

Boyi Qu, Cecile S. Bonifacio, Hasti Majidi and Klaus van Benthem

Dept. Materials Science and Engineering, University of California Davis, Davis, CA, USA

**ABSTRACT**

Increasing surface-to-volume ratios for nanoscale materials may cause metal(II)oxides phases to be thermodynamically unstable compared to their bulk counterparts. For instance, previous studies have found FeO to be unstable for nanoparticles with dimensions below 100 nm. In this study in-situ TEM was used to gradually reduce nanoparticles and nanochains of $Fe_2O_3$. Electron energy-loss spectroscopy and selected area diffraction at different temperatures not only confirm earlier predictions, but also reveal the unexpected stabilization of the FeO phase for nanochains with a minimal critical length. Hence, dimensionally constrained phases were stabilized on length-scales that were previously considered unattainable.

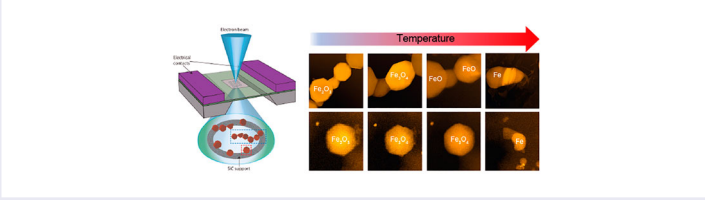


**ARTICLE HISTORY**
Received 30 July 2019

**KEYWORDS**
EELS; TEM; thermodynamic stability; nanocrystalline oxides

**IMPACT STATEMENT**

This study provides direct experimental evidence for the previously unanticipated stabilization of metal(II)oxides with dimensions well below 100 nm, which has exciting potential for catalyst technologies and next generation memory devices.

## Introduction

Nanoscale materials have exciting physical properties remarkably different from their bulk counterparts [1], including nanoscale transport processes, modified reduction–oxidation behaviors, and length-scale dependent mechanical strength. Such effects are commonly attributed to rapidly increasing surface area to volume ratio with decreasing dimensions, which causes surface thermodynamics to dominate [2]. Higher average binding energy per atom can directly impact oxidation–reduction reactions [3], solubility limits [4], and phase stability [5–7]. For spinel-type oxide nanocrystals with dimensions around 10 nm, Navrotsky et al. report shifts in redox free energies, oxygen fugacity, and stabilization temperatures when compared to the bulk. From their study the authors generally concluded that smaller surface energies for spinel structures compared to the respective divalent oxides leads to diminished thermodynamic stability [6].

Iron oxide is ubiquitous in nature, exists in various polymorphs [8], and finds application as efficient catalyst for fuel-cell reactions [9], electrode materials for rechargeable solid-state batteries [10], and nanoscale magnets [11]. In rocks, FeO serves as a redox buffer and coexists with $Fe_2O_3$ to form magnetite, in which Fe assumes oxidation states of +II and +III. Bulk FeO phase is stable above 560°C and remains metastable under ambient conditions in the multiphase configuration of magnetite [12,13]. At the nanoscale [6], FeO is replaced by a direct equilibrium between phases of metallic Fe and $Fe_3O_4$.

This study provides direct experimental evidence that nanoscale FeO is indeed thermodynamically unstable. Assembly of iron oxide nanoparticles in 1-dimensional

**CONTACT** Klaus van Benthem benthem@ucdavis.edu Dept. Materials Science and Engineering, University of California Davis, 1 Shields Ave, Davis, CA 95616, USA

Supplemental data for this article can be accessed here. https://doi.org/10.1080/21663831.2019.1684395

© 2019 The Author(s). Published by Informa UK Limited, trading as Taylor & Francis Group
This is an Open Access article distributed under the terms of the Creative Commons Attribution License (http://creativecommons.org/licenses/by/4.0/), which permits unrestricted use, distribution, and reproduction in any medium, provided the original work is properly cited.

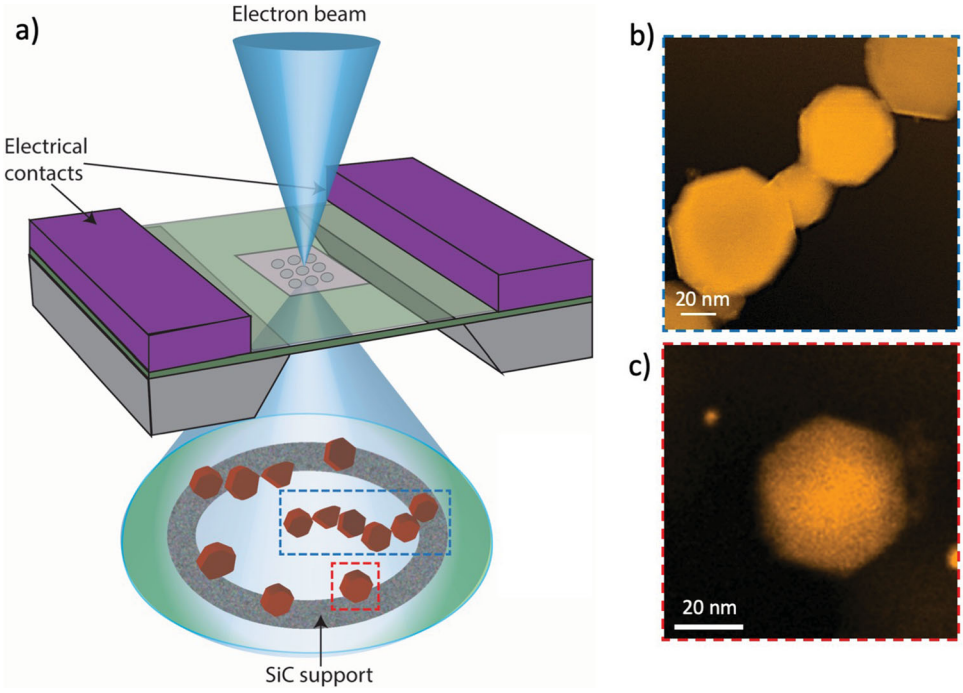


**Figure 1.** (a). Sketch of the experimental setup displaying the MEMS heating device and the incoming focused electron. Below the MEMS device is an exploded view of the sample geometry. (b) and (c) are HAADF micrographs of nanochains and isolated nanoparticles, respectively, that are supported by the SiC heating membrane.

nanochains and subsequent reduction demonstrates the ability to stabilize FeO at length scale scales below 50 nm [6]. Nanoscale stabilization of metal(II)oxides is promising for catalytic and nanometric solid state memory applications due to the existence of multiphase metal oxides [14] with complex defect structures and related physical properties [13].

## Materials & methods

In-situ transmission electron microscopy (TEM) combined with electron energy-loss spectroscopy (EELS) was used to directly observe the temperature-dependent phase stability of nanometric iron oxides, including $Fe_2O_3$, $Fe_3O_4$ and FeO. In-situ heating experiments were carried out with a Jeol JEM 2100AC aberration-corrected STEM at an oxygen partial pressure of $pO_2 = 7 \times 10^{-9}$ mbar. For in-situ heating, SiC heating membranes that are part of a micro-electro-mechanical system (MEMS) were used as TEM sample support (Figure 1a). Sample geometries included (1) individual $\gamma$-$Fe_2O_3$ nanoparticles with diameters around 46 nm dispersed onto the TEM sample support; (2) chains of interconnected nanoparticles that were collected during their synthesis above a self-sustaining diffusion flame within a homogeneous magnetic field [15]. Electron energy-loss spectra of the O K and Fe $L_{2,3}$ edges were recorded with an energy dispersion of 0.3 eV/channel. The energy resolution was around 0.9eV (FWHM of the zero-loss peak). All spectra were background subtracted using power-law fitting, and calibrated by zero-loss centering. The probe-forming convergence semi-angle was 23.4 mrad, and the collection semi-angle was approximately 15 mrad. Particle configurations were heated from room temperature to 900°C at 5°C/s. All data were recorded after holding samples for at least 10 min at the reported temperatures. Electron micrographs, energy-loss spectra, and selected area electron diffraction (SAED) patterns converged within 10 min of isothermal annealing and are thus assumed to represent thermodynamically stable configurations.

## Results & discussion

Nanoparticles and nanochains of interconnected particles were observed by high-angle annular dark field (HAADF) imaging during in-situ heating. Figure 1b and c include micrographs of typical particle configurations at room temperature. Micrographs recorded at different temperatures are included in the supplemental materials (Figure 1S). Single particles and nanochains undergo roughening transitions between 600°C and 800°C. Above 800°C sublimation of isolated particles is observed, while adjacent nanoparticles within nanochains began coarsening around 900°C (ref. [16] and Figure 1S). The different evolution of nanoparticle and nanochain

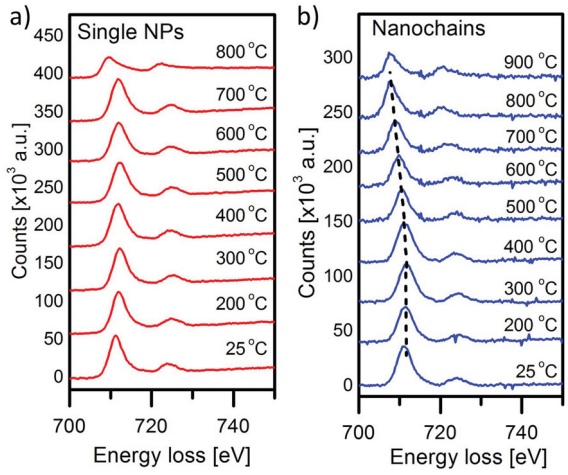


**Figure 2.** Background-stripped Fe $L_{2,3}$ edges acquired from (a) isolated particles and (b) individual nanochains after annealing to the indicated temperatures. The dotted line highlights a systematic shift of spectra towards lower energy-losses.

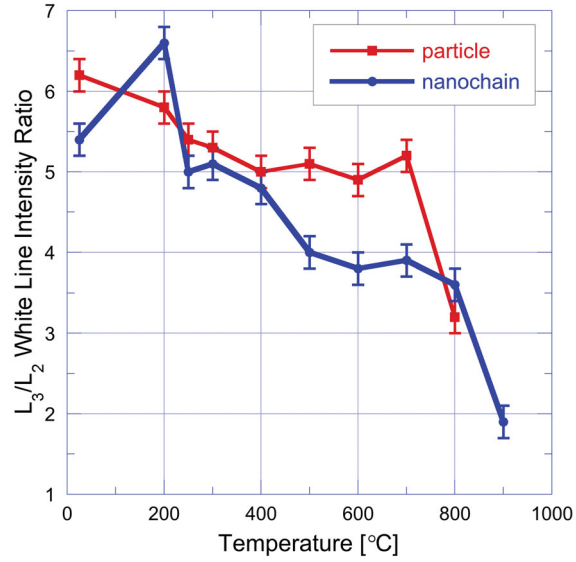


**Figure 3.** $L_3/L_2$ white line intensity ratios extracted from Figure 3 plotted as a function of temperature for both individual nanoparticles (red triangles) and nanochains (blue squares). Error bars are ±0.2.

morphologies with increasing temperature indicates a change in their redox behavior. Near-edge fine structures (ELNES) of the Fe $L_{2,3}$ absorption edges were recorded as a function of temperature to determine changes in oxidation states for Fe cations.

Figure 2 shows background stripped Fe $L_{2,3}$ edges as a function of energy loss and annealing temperature for isolated nanoparticle and nanochain configurations. For isolated particles the ELNES line shapes exhibit no significant change with increasing temperature other than a reduction of the $L_2/L_3$ intensity ratio above 700°C (Figure 2a). From nanochains, however, a reduction of the $L_2/L_3$ intensity ratios is observed at temperatures as low as 400°C. Unlike for isolated nanoparticles, the onset of the $L_3$ edge obtained from nanochains continues to shift towards lower energy losses with temperatures increasing above 400°C. For bulk iron oxides such observations are consistent with the nominal reduction of iron cations [17], hence indicating a clear difference of the reduction–oxidation behavior between individual particles and nanochains. For a more detailed identification of the apparent oxidation states, integrated $L_3/L_2$ intensity ratios were determined following a two Gaussian peak-fitting method [18]. The determined intensity ratios are plotted as a function of temperature in Figure 3. The decreasing trend in the Fe $L_3/L_2$ intensity ratio for both single nanoparticle and nanochain configurations demonstrate continuous Fe reduction with increasing temperature. Most notable is the discrepancy of the white line intensity ratios for individual nanoparticles in the temperature interval between 400°C and 800°C, where values range between 4.8 and 5.2. Ratios obtained from nanochains drop to significantly smaller values between 3.5 and 4.0. The white line intensity ratios observed in this study reproduce those from previous reports that were obtained by the same technique [17–20]. Comparison of the experimental data to reference data was subsequently used to identify specific iron oxide phases. Discrepancies between the $L_3/L_2$ intensity ratios found in this study this study and the reference data listed in Table 1 reflect systematic errors that are attributed to differences in counting statistics and EELS processing parameters, including the widths of energy intervals for spectrum integration and continuum background fitting. The observed $L_3/L_2$ intensity ratios reveal that *in situ* annealing of the iron oxide nanochains resulted in the transition from $\gamma$-$Fe_2O_3$ to $Fe_3O_4$ at 250°C, followed by FeO between 400°C and 800°C, and metallic Fe above 800°C. In contrast, individual nanoparticles maintain white line intensity ratios consistent with $Fe_3O_4$ between 250°C and 700°C, before an abrupt reduction to metallic Fe at 800°C. No evidence was detected for FeO composition in the case of isolated nanoparticles. Complete reduction to metallic Fe was confirmed for both configurations using integrated oxygen intensities indistinguishable from the experimental noise.

EELS experiments were carried out either during in-situ heating to the reported temperatures, or immediately after rapid cooling to room temperature. ELNES line shapes and their respective $L_3/L_2$ intensity ratios revealed no detectable differences, irrespective of whether they were recorded during in-situ heating or after cooling. The gradual reduction of Fe during in-situ heating indicates

**Table 1.** Reference data for $L_3/L_2$ intensity ratios assigned to specific iron oxides. The listed data were obtained with identical methods utilized in this study.

| Fe $L_3/L_2$ intensity ratio | Assigned Phase |
|---|---|
| $6.5 \pm 0.3$ | $\alpha$-$Fe_2O_3$ [19] |
| $6.0 \pm 0.3$ | $\alpha$-$Fe_2O_3$ [20] |
| $5.8 \pm 0.3$ | $\gamma$-$Fe_2O_3$ [19] |
| $5.5 \pm 0.3$ | $\gamma$-$Fe_2O_3$[17,20] |
| $5.2 \pm 0.3$ | $Fe_3O_4$[19,20] |
| $4.6 \pm 0.3$ | FeO [19] |
| $4.4 \pm 0.3$ | FeO [17] |
| 3.0 | Fe [17] |

the irreversible formation of thermodynamically stable phases for the specific experimental conditions, i.e. temperature intervals and oxygen partial pressure. Reoxidation during cooling of the sample is suppressed due to the insufficient oxygen partial pressure in the continuously pumped vacuum.

For individual nanoparticles and nanochains the phase transformation from $Fe_2O_3$ to $Fe_3O_4$ initiated at 250°C. The $Fe_3O_4$ phase was maintained up to 700°C in the case of isolated nanoparticles. Transition to the FeO phase was observed for nanochains around 400°C. Nanochains retained the FeO phase to temperatures as high as 800°C while no FeO phase was detected for isolated nanoparticles. The shape of the nanoparticles however changed from faceted to round starting at approximately 600°C before mass loss due to sublimation occurred. The presence of the FeO phase within the nanochain configuration was independently confirmed by in-situ SAED experiments. Figure 4 shows an SAED pattern and a bright field TEM image recorded from the same $Fe_2O_3$ nanochains before thermal annealing. Figure 5 shows radial intensity line profiles as a function of reciprocal lattice spacings extracted from rotationally averaged diffraction patterns that were recorded from the same nanochain at different temperatures. At room temperature (Figure 5a) observed reciprocal lattice spacings are in excellent agreement with those reported from previous SAED and X-ray powder diffraction studies for $\gamma$-$Fe_2O_3$ [21,22]. Both maghemite and magnetite ($Fe_3O_4$) crystallize with the cubic spinel structure (space group Fd-3 m), which makes it challenging to distinguish the two phases from each other. However, the relatively small particle diameters combined with the excitation error for the TEM experiments result in the appearance of kinetically forbidden diffraction spots, including the (211) peak observed at room temperature (Figure 5a) which is exclusive for $\gamma$-$Fe_2O_3$. Its absence from the SAED patterns recorded at 600°C (cf. Figure 5b) provides evidence for the phase transformation from $\gamma$ -$Fe_2O_3$ to $Fe_3O_4$. SAED patterns recorded after continuous heating to 800°C exhibit significantly different distributions of diffraction intensities. Figure 5c reveals peak intensities that are in excellent agreement with {111}, {200}, and {220} lattice planes in FeO. The small remanence of diffraction intensities coinciding with {222}, {400}, and {511} reflections in $Fe_3O_4$ suggest a gradual transformation of the nanochains from $Fe_3O_4$ to FeO. Such transformation kinetics are expected since the three iron oxides are comprised of similar closed packed arrays of oxygen anions, in which iron cations can easily move between octahedral and tetrahedral sites. It was previously reported that free surface activities change as a function crystallographic orientation [23–25], which suggests that different facets of the nanoparticles will obey slightly different reduction kinetics. SAED patterns recorded at 900°C are in excellent agreement with those expected for metallic $\gamma$ -Fe (cf. Figure 5d). The TEM micrograph in the inset of Figure 5d demonstrates sintering of nanochains.

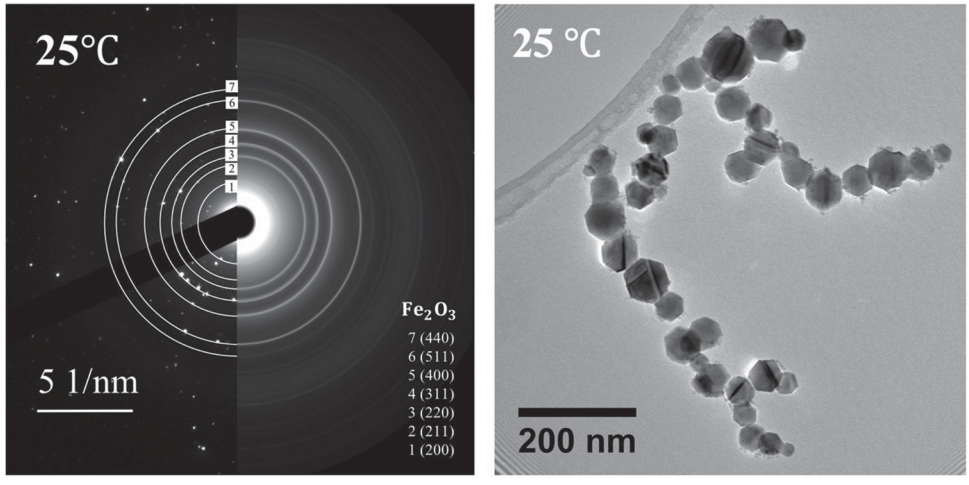


**Figure 4.** SAED pattern and bright field TEM image of $\gamma$-$Fe_2O_3$ nanochains recorded before thermal annealing at 25°C. For more accurate determination of reciprocal lattice spacings SAED patterns were rotationally averaged.

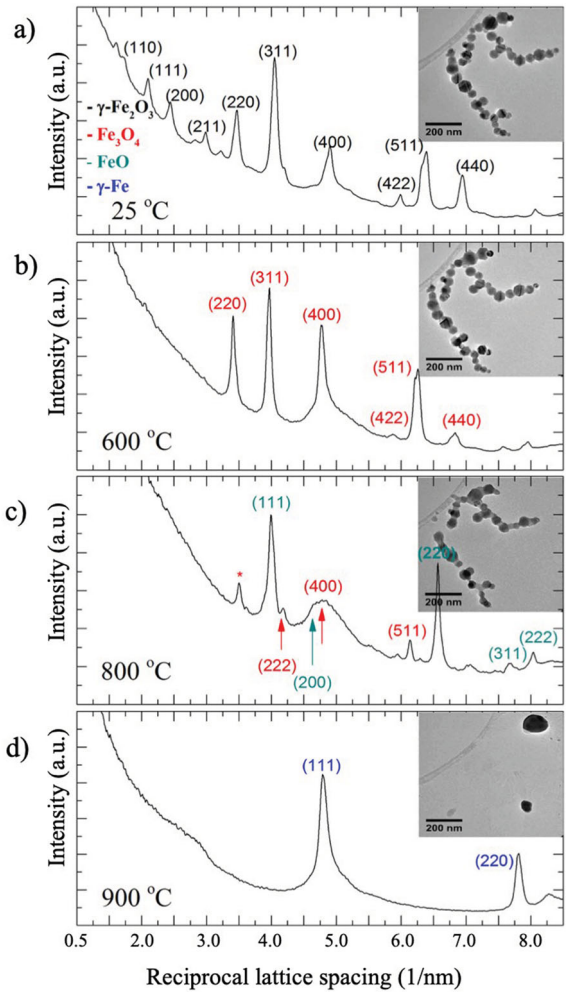


**Figure 5.** Rotationally average reciprocal lattice spacings extracted from SAED patterns recorded between 25°C and 900°C. Lattice spacings for $\gamma$-$Fe_2O_3$, $Fe_3O_4$, Fe, and metallic Fe are labeled with respective Miller indices.

EELS and SAED experiments during in-situ annealing directly confirm stabilization of the FeO phase on the nanoscale provided nanoparticles are arranged in nanochain configurations. This result is remarkable since the FeO phase remains confined within 50–70 nm in two independent directions, while phase stabilization is accommodated by interconnecting adjacent particles.

Navrotsky et al. [6] have argued that differences in surface energies have a strong influence on phase stability by shifting redox free energies by up to 30 kJ/mol. Size-driven thermodynamic crossovers in phase stability at the nanoscale are a result of the changes in the free energies of polymorphs due to differences in surface energies [6,26–29]. Thermodynamic calculations have predicted that isolated FeO nanoparticles with diameters below 100 nm are unstable and $Fe_3O_4$ and Fe phases coexist [6]. The EELS results for isolated particles observed in this study provide direct experimental evidence for the coexistence of $Fe_3O_4$ and Fe. Temperatures as low as 400°C, however, reveal the stabilization of the FeO phase for nanochains with lengths equivalent to 6–8 particle diameters. The assembly of individual nanoparticles into chain-like geometries and partial sintering between particles (Figure S1 and reference [16]) leads to the formation of particle/particle contacts with grain boundary energies lower than the specific surface energies. This effect alongside potential particle rotation and faceting decreases the total surface energy of the particle ensemble and stabilizes the FeO phase.

EELS data recorded from nanochains consisting of less than 4 interconnected particles did not reveal any FeO formation at temperatures as high as 700°C. Instead, magnetite transformed directly to the metal phase, indicating that nanochains of at least 4 particles, or an equivalent length of about 180 nm are required to stabilize FeO. Considering particle diameters of 46 nm, and interparticle neck diameters around 24–26 nm (see Figure S1), surface to volume ratios of nanochains comprising of at least 6 nanoparticles are 12–14% smaller than those observed for individual nanoparticles of the same size. Surface to volume ratios for 6-particle nanochains are similar to those of individual nanoparticles with diameters around 50–60 nm, potentially suggesting that particle sizes considerably smaller than those previously estimated may present stability of FeO. Purely geometric arguments in conjunction with earlier analysis of redox phase equilibria [6] suggest that the stabilization of metal(II)oxide phases in nanochain configurations may be a general phenomenon not restricted to only iron oxides. Phase stability for CoO was reported during reduction reactions of thin films [30]. The relatively low $Fe_3O_4$ to FeO transition temperature of 400°C is consistent with previous indirect observations for thin metal–oxide films [31].

The results of this study demonstrate the potential to stabilize metal(II)oxides on length scales where they were previously considered unstable. For individual nanoparticles, the stability of metal(II)oxides is inhibited by the larger total surface energy. At the nanoscale increasing surface area to volume ratios can be considered as extra pressure due to increased surface tension, which makes the formation of metal(II)oxides energetically unfavorable compared to 1-dimensional nanochains. The relatively smaller grain boundary energies compared to free surface energies further suggest the ability to similarly stabilize microstructures of nanocrystalline metal(II)oxides. A prediction of critical nanochain length however requires consideration of free surface energies, specific grain boundary energies, redox potentials and oxygen partial pressures. The ability to stabilize nanoscale metal(II)oxides, and especially FeO, will enable applications in nano-magnetic and

catalyst technologies for next generation memory devices and more efficient hydrogenation of nitroarenes during the manufacturing of pharmaceuticals and agricultural chemicals.

## Acknowledgement

This work was supported by the US National Science Foundation (grant DMR-0955638), the Army Research Office under grants #W911NF-12-10491 (program manager Dr. David Stepp), and #W911F-16-1-0364 (program manager: Dr. Michael Bakas). The authors acknowledge invaluable discussions with G. Das, I. Kennedy, and A. Navrotsky.

## Disclosure statement

No potential conflict of interest was reported by the authors.

## Funding

This work was supported by the US National Science Foundation (DMR-0955638), the Army Research Office under grants #W911NF-12-10491 (program manager Dr. David Stepp), and #W911F-16-1-0364 (program manager: Dr. Michael Bakas).

## ORCID

*Klaus van Benthem* http://orcid.org/0000-0001-8865-046X

## References

[1] Pan ZW, Dai ZR, Wang ZL. Nanobelts of semiconducting Oxides. Science. American Association for the Advancement of Science; 2001 Mar 9;291(5510):1947–1949.
[2] Roduner E. Size matters: why nanomaterials are different. Chem Soc Rev. 2006;35(7):583.
[3] Matsuno M, Bonifacio CS, Rufner JF, et al. In situ transmission electron microscopic investigations of reduction-oxidation reactions during densification of nickel nanoparticles. J Mater Res. 2012;27(18):2431–2440.
[4] Lee JG, Mori H. Solid solubility in isolated nanometer-sized alloy particles in the Sn-Pb system. Eur Phys J D. 2005 Jul 13;34(1-3):227–230.
[5] Wautelet M. Estimation of the variation of the melting temperature with the size of small particles, on the basis of a surface-phonon instability model. J Phy D-Appl Phy. 1991;24:343–346.
[6] Navrotsky A, Ma C, Lilova K, Birkner N. Nanophase transition metal oxides show large thermodynamically driven shifts in oxidation-reduction equilibria. Science. American Association for the Advancement of Science; 2010 Oct 8;330(6001):199–201.
[7] Bajaj S, Haverty MG, Arróyave R, et al. Phase stability in nanoscale material systems: extension from bulk phase diagrams. Nanoscale. 2015;7(21):9868–9877.
[8] Samsonov GV. The oxide handbook. American Edition. New York (NY): IFI/Plenum; 1973.
[9] Harris RA, Shumbula PM, van der Walt H. Analysis of the interaction of surfactants oleic acid and oleylamine with iron oxide nanoparticles through molecular mechanics modeling. Langmuir. 2015 Apr 7;31(13):3934–3943.
[10] Qi X, Xu J, Zhong W, Du Y. A facile route to synthesize core/shell structured carbon/magnetic nanoparticles hybrid and their magnetic properties. Mater Res Bull. 2015 Jul;67:162–169.
[11] Harshiny M, Iswarya CN, Matheswaran M. Biogenic synthesis of iron nanoparticles using Amaranthus dubius leaf extract as a reducing agent. Powder Technol. 2015 Dec;286:744–749.
[12] Darken LS, Gurry RW. The system Iron—Oxygen. II. Equilibrium and thermodynamics of Liquid oxide and other phases. J Am Chem Soc. 1946 May;68(5):798–816.
[13] Chen C-J, Chiang R-K, Lai H-Y, Lin C-R. Characterization of Monodisperse Wüstite nanoparticles following partial oxidation. J Phys Chem C. 2010 Mar 18;114(10):4258–4263.
[14] Minervini L, Grimes RW. Defect clustering in wüstite. J Phys Chem Solids. 1999 Feb;60(2):235–245.
[15] Das GK, Bonifacio CS, De Rojas J, Liu K, van Benthem K, Kennedy IM. Ultra-long magnetic nanochains for highly efficient arsenic removal from water. J Mat Chem A. Royal Soc Chem; 2014;2(32):12974–12981.
[16] Bonifacio CS, Das G, Kennedy IM, van Benthem K. Reduction reactions and densification during in situTEM heating of iron oxide nanochains. J Appl Phys. 2nd ed. 2017 Dec 21;122(23):234303.
[17] Leapman RD, Grunes LA, Fejes PL. Study of the L23edges in the 3d transition metals and their oxides by electron-energy-loss spectroscopy with comparisons to theory. Phys Rev B [Internet]. American Physical Society; 1982;26(1):614–635. Available from: https://journals.aps.org/prb/abstract/10.1103/PhysRevB.26.614
[18] Jasinski J, Pinkerton KE, Kennedy IM, Leppert VJ. Spatially Resolved energy electron loss spectroscopy studies of iron oxide nanoparticles. Microsc Microanal. Cambridge University Press; 2006 Oct 1;12(5):424–431.
[19] Colliex C, Manoubi T, Ortiz C. Electron-energy-loss-spectroscopy near-edge fine structures in the iron-oxygen system. Phys Rev B. American Physical Society; 1991 Nov 15;44(20):11402–11411.
[20] Pearson DH, Fultz B, Ahn CC. Measurements of 3d state occupancy in transition metals using electron energy loss spectrometry. Appl Phys Lett. AIP Publishing; 1988 Oct 10;53(15):1405–1407.
[21] Kim W, Suh C-Y, Cho S-W, et al. A new method for the identification and quantification of magnetite–maghemite mixture using conventional X-ray diffraction technique. Talanta. Elsevier; 2012 May 30;94:348–352.
[22] Ding Y, Morber JR, Snyder RL, Wang ZL. Nanowire structural evolution from $Fe_3O_4$ to $\varepsilon$-$Fe_2O_3$. Adv Funct Mater. John Wiley & Sons, Ltd; 2007 May 7;17(7):1172–1178.
[23] Li W, Yang KR, Yao X, et al. Facet-dependent kinetics and energetics of hematite for solar water oxidation reactions. ACS Appl Mater Interfaces. American Chemical Society; 2018 May 24;11(6):5616–5622.
[24] Lee I, Delbecq F, Morales R, et al. Tuning selectivity in catalysis by controlling particle shape. Nat Mater. Nature Publishing Group; 2009 Feb 1;8(2):132–138.
[25] Tian N, Zhou ZY, Sun SG, et al. Synthesis of tetrahexahedral platinum nanocrystals with high-index facets and high electro-oxidation activity. Science. American Association for the Advancement of Science; 2007 May 4;316(5825):732–735.

[26] Navrotsky A, Mazeina L, Majzlan J. Size-driven structural and thermodynamic complexity in iron oxides. Science. American Association for the Advancement of Science; 2008 Mar 21;319(5870):1635–1638.
[27] McHale JM, Auroux A, Perrotta AJ, et al. Surface energies and thermodynamic phase stability in nanocrystalline Aluminas. Science. American Association for the Advancement of Science; 1997 Aug 8;277(5327):788–791.
[28] Ranade MR, Navrotsky A, Zhang HZ, et al. Energetics of nanocrystalline $TiO_2$. Proc Natl Acad Sci U S A. Nat Acad Sci. 2002 Apr 30;99(suppl 2):6476–6481.
[29] Navrotsky A. Calorimetry of nanoparticles, surfaces, interfaces, thin films, and multilayers. J Chem Thermodyn. 2007 Jan;39(1):1–9.
[30] Papaefthimiou V, Dintzer T, Dupuis V, et al. Nontrivial redox behavior of Nanosized Cobalt: new insights from ambient pressure X-ray Photoelectron and absorption spectroscopies. ACS Nano. 2011 Mar 22;5(3):2182–2190.
[31] Bertram F, Deiter C, Pflaum K, et al. In-situ x-ray diffraction studies on post-deposition vacuum-annealing of ultra-thin iron oxide films. J Appl Phys. 2011;110(10):102208.